Solubility Trapping as a Potential Secondary Mechanism for CO2 Sequestration during Enhanced Gas Recovery by CO_2 Injection in Conventional Natural Gas Reservoirs: An Experimental Approach

Muhammad Kabir Abba[1], Abubakar J. Abbas[1], Athari Al-Otaibi[1] Ghasem G. Nasr, Martin L. Burby[1], Bello Saidu[1], Salihu W. Suleiman[1]

Journal of Natural Gas Science and Engineering

1 The University of Salford Manchester UK

ABSTRACT

This study aims to experimentally investigate the potential of solubility trapping mechanism in increasing CO_2 storage during EGR by CO_2 injection and sequestration in conventional natural gas reservoirs. A laboratory core flooding process was carried out to simulate EGR on a sandstone core at 0, 5, 10wt% NaCl formation water salinity at 1300 psig, 50^{o}C and 0.3ml/min injection rate. The results show that CO_2 storage capacity was improved significantly when solubility trapping was considered. Lower connate water salinities (0 and 5 wt%) showed higher CO_2 solubility from IFT measurements. With 10% connate water salinity, the highest accumulation of the CO_2 in the reservoir was realised with about 70% of the total CO_2 injected stored; an indication of improved storage capacity. Therefore, solubility trapping can potentially increase the CO_2 storage capacity of the gas reservoir by serving as a secondary trapping mechanism in addition to the primary structural and stratigraphic trapping and improving CH_4 recovery.

1 INTRODUCTION

The incessant utilisation of fossil fuels as sources of energy invariably increases greenhouse gases (GHG) emissions in the atmosphere and eventually lead to the proliferation of global warming. The reduction of these GHG emissions has become paramount, and it is gaining significant attention globally due to its environmental consequences. The main component of the GHGs responsible for nearly 64% of the accrued negative effect on the environment is CO_2 (Ding et al., 2018). Thus, reduction of this anthropogenic CO_2 emission cannot be overemphasised. Carbon Capture technology is a potential approach to reducing the CO_2 emissions from heavy industries (Ding et al., 2018; Li et al., 2013; Pereira et al., 2017) followed by the geological/underground storage and sequestration of the captured CO_2 (Burton et al., 2009; Ganjdanesh and Hosseini, 2017; Mijic et al., 2014; Mutailipu et al., 2018a). In all the underground storage sites, oil and gas reservoirs have the potential or appeal to provide additional throughput in the form of economic incentives (Ding et al., 2018; Kalra and Wu, 2014). These incentives are realised through enhanced recovery techniques – miscible flooding technique in enhanced oil recovery and CO_2 injection in enhanced gas recovery processes. However, natural gas reservoirs have the upper hand in terms of potential and practicality storage compared to the oil reservoirs due to their existing gas storage capability (Ding et al., 2018). Gas reservoirs have stored natural gas for long periods of time safely without the penchant for surrounding leaks. The extraction of gas from conventional natural gas reservoirs does not require complex processes of altering the reservoir matrix to enhance its production because primary recovery can be in excess of 80% (van der Meer, 2005) depending on the drive mechanism. Oil reservoirs, on the other hand, must be subjected to an array of complex process

through artificial stimulation techniques like hydraulic fracturing or matrix acidizing in order to enhance the production which in turn tends to affect the reservoir integrity, and a potential CO_2 leakage and contamination of adjacent freshwater aquifers will ensue overtime as emphasised by (Xiao et al., 2016). CO_2 is a medium for the mobilisation of oil in the reservoir during tertiary recovery and the risk associated with the leaks is the transportation of complex organic compounds present in the crude oil like benzene, toluene, ethylbenzene and xylenes (BTEX) which are highly toxic (Cantrell and Brown, 2014) into adjacent aquifers through fissures and fracture propagation resulting from recovery techniques. This reason, among others as pointed in the works of Kalra et. al. (2014), highlights the choice of natural gas reservoirs as potential sequestration site for anthropogenic CO_2 emissions albeit the current natural gas market compared to oil prices from an economic standpoint. Nonetheless, the drive to exploit the economic viability of EGR through understanding the physics of mixing between the injected CO_2 and the recovered CH_4 and its minimisation should be upheld.

Accordingly, conventional natural gas reservoirs have a storage capacity limitation compared to the most ideal choice i.e. deep saline aquifers (Sminchak et al., 2017) for CO_2 sequestration. Deep saline aquifer utilises a combination of different trapping mechanisms (structural and stratigraphic, solubility, residual, mineral) to store the injected CO_2 and as such increases, significantly, its storage potential. Conversely, the primary trapping mechanism for CO_2 in conventional natural gas reservoirs is structural trapping owing to the geological seals of the reservoir (cap rock) which prevents the natural resource from migrating to the upper strata of the overlying formations and in this case the injected CO_2. However, an additional trapping mechanism that can be explored to further improve the storage capacity of the conventional natural gas reservoir i.e. the solubility trapping mechanism of the CO_2 in the formation water. This can potentially be exploited in tandem with the primary trapping mechanism to increase the storability of the natural gas reservoir. As a secondary CO_2 geological trapping mechanism post injection time (Li et al., 2013), significant volume of CO_2 can be dissolved and stored in the formation water given the high solubility of CO_2 in water. In most cases, solubility trapping mechanism in the purview of CO_2 storage is usually associated, investigated, and adapted in deep saline aquifers alone (Chen et al., 2018; Ding et al., 2018; Jia et al., 2017; Li et al., 2013; Nakajima and Xue, 2017; Oh et al., 2017; Raza et al., 2016; L M Valle et al., 2018; L.M. Valle et al., 2018). Experimental investigation of solubility trapping mechanism in unconventional natural gas reservoirs during EGR is, to the author's knowledge, limited and the practicality of its effectiveness in this regard needs to be evaluated to further present its potential as a viable option for CO_2 sequestration.

Furthermore, CO_2 displaces CH_4 during EGR by advection or diffusion mechanism where displacement is either controlled by interstitial velocity or concentration gradient, unlike EGR by CO_2 injection in unconventional natural gas reservoirs, like coal bed methane and shale gas, whose mechanisms of displacement are desorption of the CH_4 and adsorption of CO_2 where selective adsorption depends on the clay content of the rock (Duan et al., 2016). This displacement mechanism in EGR for this study is quintessential to the assessment of the storability of the injected CO_2 and the recovery of the nascent CH_4 and the interplay between them in the conventional reservoir. The influence of the connate water salinity and its presence in the conventional natural gas reservoir during EGR has already been established in our previous

work (Abba et al., 2018). Therefore, this study aims to highlight, experimentally, the feasibility of solubility trapping, in addition to structural trapping, as a secondary trapping mechanism during enhanced gas recovery by CO_2 injection and assess its potential to increase the storage capacity of the reservoirs with respect to natural gas recovery efficiency in conventional sandstone reservoirs.

2 MATERIALS AND METHOD

In this study, a core flooding experiment was carried which involved the injection of CO_2 through a core sample saturated with CH_4 and connate water at different salinities. The core sample used was *Grey Berea* sandstone with petrophysical properties and dimensions as shown in Table 1. The salinities of the connate water used were 0, 5, 10wt% NaCl.

Table 1 Core sample dimensions and petrophysical properties

Core sample	Length (mm)	Diameter (mm)	Porosimetry Porosity (%)	Gas Permeability (mD)
Grey Berea	76.27	25.22	20.3	217

2.1 Materials

High purity Carbon Dioxide and Methane with purities of >99.999% were used and sourced from BOC UK which is a member of Linde Group. The core sample was acquired from Kocurek USA. General purpose NaCl salt used in this study was supplied by Fisher Scientific UK.

2.2 Experimental Method

A series of experiments were carried out to achieve the aim set out in this study. The core sample was first characterised to evaluate the petrophysical properties of the core sample for concise and dependable measurements of the parameters under investigation. Brines of different test salinities were prepared which were used for the investigation. After these preliminary preparatory tasks were carried out, a core flooding process was conducted on the core sample to evaluate the displacement efficiency of the process in the presence of the test connate water prepared. 5 tests for individual brine concentrations were carried out. The effluent compositions were analysed using gas chromatography at different time intervals using the configured sampling valve. Details of the procedure and set up are presented in our earlier work (Abba et al., 2017). The effluent rates were measured and recorded by the downstream flow meters. These provided the volumes produced by displacement of CH_4 by the injected CO_2 and paved a way to quantify the trapped or stored CO_2 in the core sample after substantial recovery of the desired CH_4. The solubility through interfacial interaction between the different gases in different brine salinities

for all the experiments was studied using the rising bubble method of interfacial tension measurement. Details of the experimental set up and procedure is shown in section 2.2.4.

2.2.1 Brine preparation

The connate water of different salts concentration was prepared in a round bottom flask with a magnetic stirrer on a magnetic plate. The stirring was kept at a medium rate as precautionary measure to obtain a homogeneous solution of the brine where all the solute was fully dissolved. Two brines of 5, 10 wt% NaCl concentrations were prepared to simulate the formation water salinities for the investigation.

2.2.2 Core sample saturation

For this study, 10% of characterised core sample was then saturated with the distilled water and prepared brines (5, 10wt%) to represent the connate water using the vacuum saturation method. Given the nature of the core sample used and the core flooding equipment, 10% saturation was ideal as it provided sufficient surface area for the fluid-rock interaction within the pore matrix. Furthermore, it reduced the risk of damage to the core holder, back pressure regulator and tubing of the core flooding equipment from the acidic effluents formed by the interaction of the supercritical CO_2 and the simulated connate water. Equivalent volume to 10% of the pore volume of the core sample of the tests brines was injected using the set-up in Figure 1 under vacuum to establish the connate water saturation in the core sample.

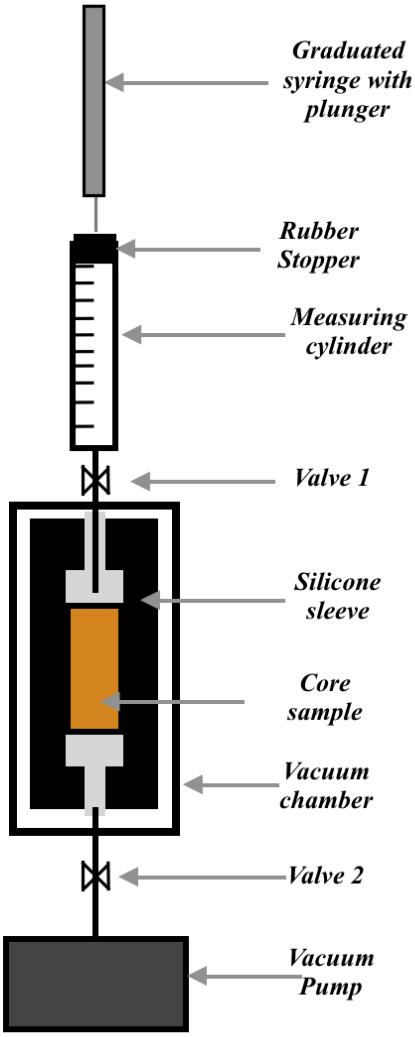

Figure 1 Vacuum saturation set up

2.2.2.1 Apparatus and procedure

Saturation set up shown in Figure 1. To carry out the saturation process, an equivalent volume of 10% of the core sample's pore volume of brine is measured out and placed in a hydrophobic syringe. The core sample (dried and weighted) was placed in the air tight sleeve in the vacuum chamber. Valve 1 was shut and valve 2 was open and the vacuum pump was run. Valve 2 was then shut off and valve 1 was opened and the brine was injected and valve 1 was shut off. The set up was allowed to sit for 4 hours. Slowly, the vacuum pressure was released, by opening the valve 2, and brought the chamber to atmospheric pressure. The now saturated core sample was weighed to verify the saturated volume. The saturated core sample was then prepared by wrapping it in cling film and foil paper. The cling film helps in preventing the foil paper from sticking to the core sample which makes it difficult to remove and clean while the foil paper help to preserve the *vitton* sleeve integrity by reducing the permeation of the supercritical CO_2 from the core sample through the sleeve. This CO_2 permeation can also cause overburden pressure fluctuations, in that the CO_2 passes through the vitton sleeve into the annulus of the core holder set-up housing the hydraulic oil which simulates the overburden pressure on the core sample.

Prior to every experiment, the core sample was cleaned using Soxhlet extraction were a reflux of methanol cycles was used to remove any traces of inorganic compounds (in this case NaCl salts) to restore the original state of the core sample for consistency. Drying in the oven at 100^{o}C overnight followed. This ensured the removal of any moisture and reagents used in the cleaning process.

2.2.3 Core flooding process

The core flooding process was carried out at 1300 psig and 0.3 ml/min injection rate using the set up shown in Figure 2 (the pressure was considered based on the gas zone density of 0.22 psi/ft, and the injection rate was from our previous work). And as aforementioned, the CO_2 injection was done employing the same procedure, operational conditions and equipment details used in our previous work (Abba et al., 2017). The set-up works based on the principle of Darcy law which defines fluid flow in porous media and its schematics is shown in Figure 2. An unsteady state flow was adopted to evaluate the mass balance between the injected CO_2 and the effluents realised – which comprised of the displaced CH_4 and the injected CO_2. The concentration profile was measured and recorded at 4-5 minutes intervals with the corresponding effluent flowrates. And the run came to an end when there were insignificant volumes of CH_4 in the produced effluents.

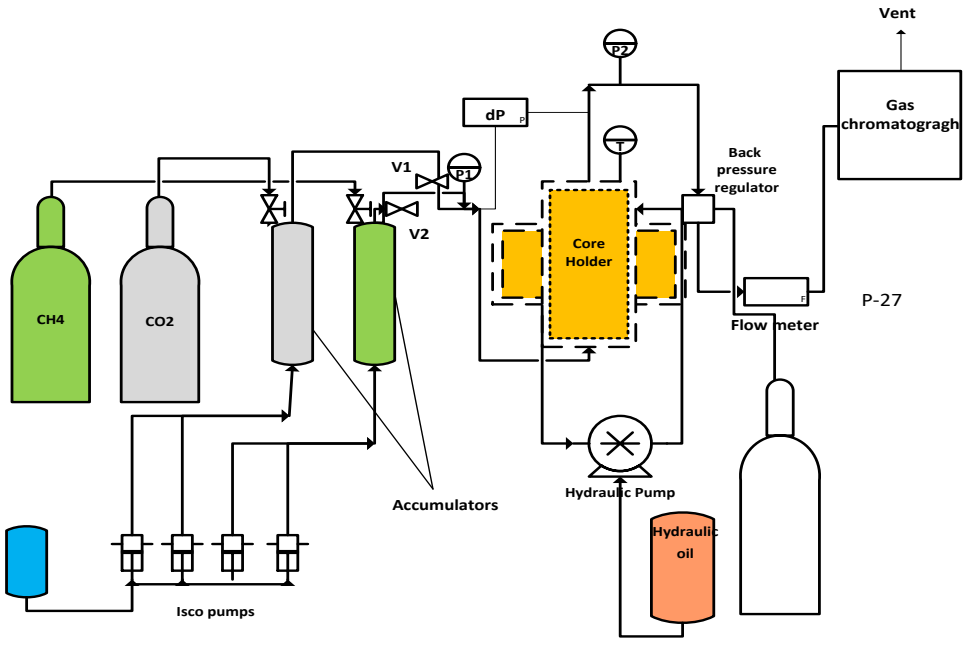

Figure 2 Schematics of core flooding set up

2.2.4 Interfacial tension measurement (IFT)

Several works have been carried out to measure the interfacial tension in CO_2-brine, CH_4-brine, CO_2-brine-CH_4 systems at different conditions (Amin et al., 2010; Arabloo et al., 2016; Bagalkot et al., 2018; Barati-Harooni et al., 2016; Chow et al., 2016; Dehghan et al., 2015; Duchateau and

Broseta, 2012; Kamari et al., 2017; Kashefi et al., 2016; Khaksar Manshad et al., 2016; Mohammad Salehi et al., 2017; Mutailipu et al., 2018a, 2018b; Pereira et al., 2017; Rashid et al., 2017; Stukan et al., 2012; Yasuda et al., 2015) and the relationship between the interfacial tension and solubility highlighted. These investigations have shown that the forces that exist at the interfaces between two phases or fluids interacting are a function of the densities, the temperature and pressures of the fluids system. And there exist mass transfer between the phases in contact which can be well attributed to the solubility of one species of the fluids in another.

2.2.4.1 Apparatus and procedure

Here, the interfacial tension measurement was done to assess the dissolution of the injected CO_2 for the duration of CH_4 displacement for EGR as a result mass transfer between the phases. Each connate water solution with a specific concentration was used to measure the IFT between the connate water and the gases at the core flooding conditions of 1300 psig and 50^{o}C. The rising bubble technique was used to carry out the measurement using the set up as shown in Figure below. A Corelab high pressure high temperature surface energy experimental set up was used. It comprised of the high pressure measurement cell which can withstand pressures of up to 10,000 psig, a Rame-Hart optical system with digital image processing software used for the IFT determination using image analysis of the bubble, a high pressure HiP 62-6-10 manual pump with a pressure rating of 10,000 psig for charging the external phase (brine) and a Temco temperature controller. The IFT is measured using DropImage software which uses a theoretical algorithm to evaluate the parameter based on the bubble profile generated.

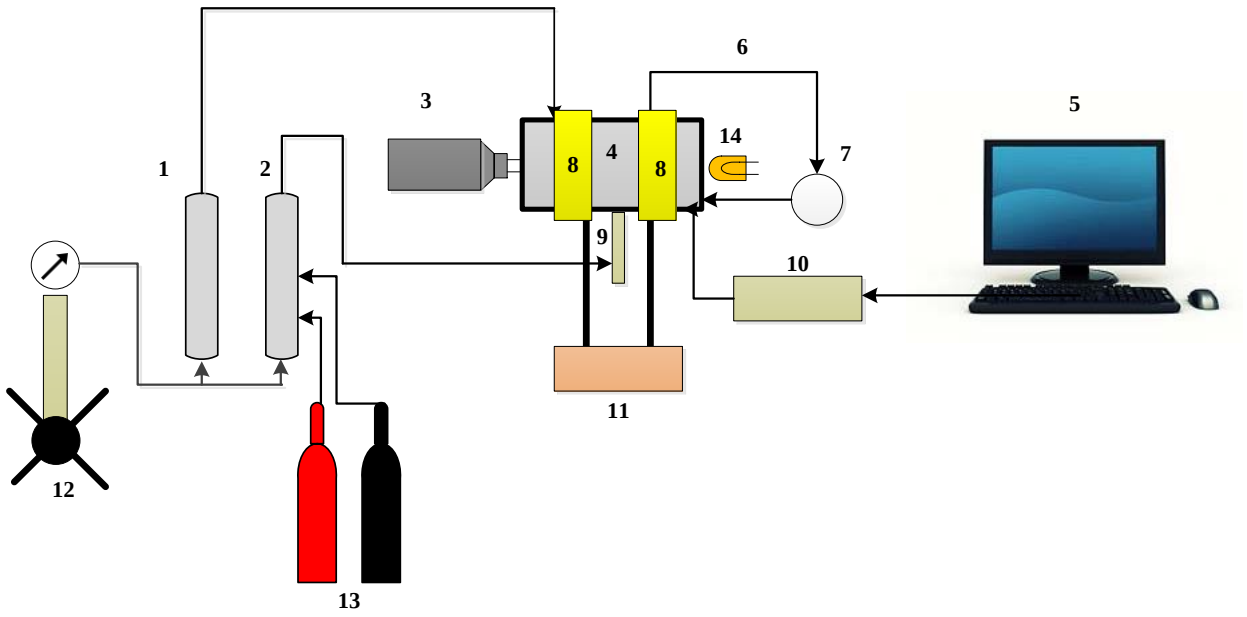

Figure 3 IFT set up - (**1&2**) accumulators (**3**) Rame-Hart digital camera (**4**) IFT cell (**5**) Monitor (**6**) Vent Valve (**7**) Vacuum Valve (**8**) Heating element (**9**) Injection Needle (**10**) data logger and temperature controller (**11**) stability controller (**12**) manual pump (**13**) gas bottles (CH_4 and CO_2) (**14**) Light source

Before the measurements, precautionary steps were taken to rid the system of any contaminant and ensure proactive experiments in obtaining reliable results. The accumulators (1&2), the IFT cell (4), the injection needle (10), the delivery tubing was soaked in acetone for 2 hours, and this step was repeated for all new samples being investigated. These components were coupled back together and then evacuated using vacuum pump (8). Hot distilled water was then placed inside the accumulators and then injected into IFT cell to flush the whole system. Dry compressed air was then used to dry the entire system in preparation for the IFT measurements.
The external phases (brine/distilled water) were charged into the cell using the manual pump till the desired pressure was attained and also the temperature was set using Corelab temperature controller with an accuracy of ±0.3^{o}C as the system pressure was set in order to maintain the temperature at the desired temperature. After the pressures and temperatures have stabilised, the gases (CH_4 or CO_2) were then introduced into the drop phase accumulator. Then the manual pump was used to pressurise the gas in the accumulator to the desire test pressures slightly above the cell pressure. Creating the bubble inside the test cell was done by gently opening the injection needle valve and monitoring the development of the bubble. The bubble development and collapse were recorded using the DropImage software based on the Young-Laplace equation. Details of which are discussed in Section 3.1.3.

This bubble measurement was repeated for 4 bubbles in each experiment for repeatability and acquired data reliability and the IFT measurement was made repeatedly on each bubble image obtained.

3 RESULTS AND DISCUSSION

3.1 Core flooding experiment

The recovery efficiency of the experiment was investigated using a laboratory simulated displacement experiment to determine the concentration profiles of the interacting gas species. This entailed injection of the CO_2 into the core sample saturated with CH_4 and connate water. As already mentioned in Section 2.2, a number of test runs were carried out to assess the repeatability of the experimental methodology and set up and the error analysis for the best three runs prior to the actual runs were selected and shown in the appendix.

3.1.1 Methane Recovery

First, the CH_4 produced was evaluated based on the total volume of effluents produced after the core flooding experiment was stopped. These volumes were fractions of the original gas in place in the core sample. The results obtained are presented in Table 2 below.

Table 2 CH_4 production in pore volumes for all the runs

Time (min)	**PV Produced 10 wt% CH_4**	**Time (min)**	**PV Produced 5 wt% CH_4**	**Time (min)**	**PV Produced Distilled CH_4**	**Time (min)**	**PV Produced Dry CH_4**
0.17	2.03	0.17	5.13	0.15	7.07	0.16	7.02
5.32	8.31	5.33	21.13	5.49	23.62	5.33	27.82
10.66	9.16	10.67	24.00	10.83	26.27	10.67	29.64

15.99	9.57	15.82	17.12	15.99	10.82	15.83	9.94
21.16	9.90	21.16	7.78	21.32	7.27	21.16	6.86
26.49	3.15	26.49	3.86	26.66	5.10	26.49	5.63
31.66	1.63	31.83	2.70	31.98	3.35	31.82	4.97
37.01	1.16	37.16	1.86	37.16	2.46	37.16	4.53
42.32	0.89	42.33	1.15	42.48	1.91	42.32	4.17
47.66	0.57	47.67	0.58	47.82	1.17	47.82	3.75
53.82	0.31	53.33	0.41	55.98	0.35	54.66	3.31
59.16	0.18	59.49	0.41	61.33	0.11	60	2.99
64.32	0.19	65.16	0.42	66.66	0.08	65.16	2.85

These results are presented in a graphical form in Figure 4 which shows the trends observed. As can be seen, the poorest CH_4 recovery in all the runs was realised in the run where 10 wt% of connate water was used. This can be attributed to the poor sweep efficiency of the injected because of the restrictive flow when CO_2 traverses the core sample. This restriction is as a result of the higher salinity (high density) connate water sealing off the narrower pore spaces within the pore matrix due to its density compared to the other runs with lower connate water concentration with lower densities. Because of the forced-homogeneity actualised by the presence of the connate water in the pore matrix, less time was spent by the CO_2 as it was injected through the core sample and also early CO_2 breakthrough as seen in the concentration profile in Figure 5.

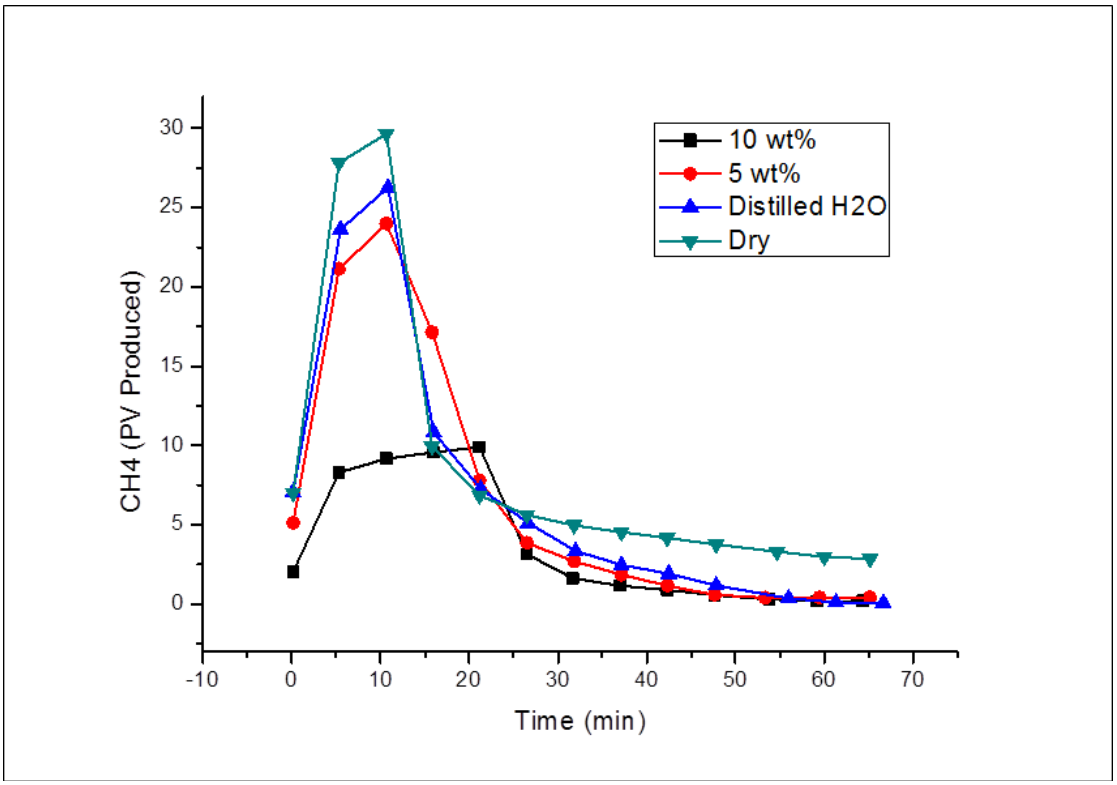

Figure 4 Graphical representation of CH4 volumes produced from all the experiments

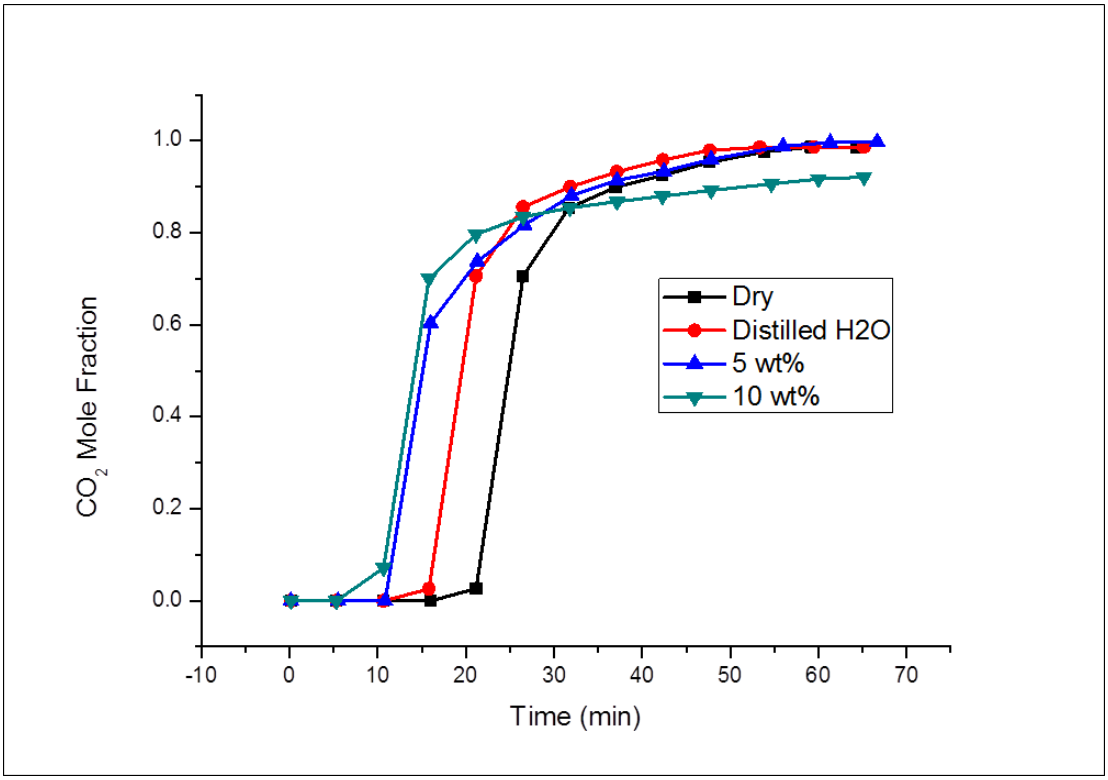

Figure 5 Concentration profiles of CO_2 produced

The original gas in place (OGIP) in the core sample before the commencement of the flooding process was obtained using the same relation in Eq. 1 as employed in our previous work (Abba et al., 2018).

$$G = \frac{v_b \phi (1 - S_w)}{B_g} \quad (1)$$

Where G is the original gas in place in scm^3, v_b is the bulk volume in cm^3, Sw is initial water saturation fraction, Bg is gas formation volume factor in cm^3/scm^3 for the purpose of this research. This was then used to evaluate the CH_4 recovery factor shown in Table 3.

Table 3 CH_4 recovery factor evaluation for each test

Tests	Swi (%)	CH_4 Produced PV	OGIP PV	Recovery Factor (%)
10wt%	10	13.62	82.87	16.44
5wt%	10	53.11	82.87	64.09
Distilled	10	56.17	82.87	67.78
Dry	0	81.55	83.23	97.98

Furthermore, the CH_4 recovery was highest when there was no connate water saturation. This is obvious because there was no reduction in the original pore volume for the gas to occupy and hence more volume for nascent CH_4. Higher volume of CH_4 was realised in the core sample during the dry run and thus higher recovery was observed. This will serve as the benchmark to

which other tests are pitted against. So, analysis will be accentuated in the runs with 10% of their pore volumes saturated with connate water of different salinities (0, 5, 10 wt%). The concentration profile also presented, notably, the variation of the breakthrough times with the salinities. This variation was explained in our previous works where significant pressure drop was seen when CO_2 was displacing CH_4 at a 10wt% connate condition (Figure 6). The same restrictive flow comes into play when explaining the variation in breakthrough times. The higher the salinity of the connate water the more pore throat sealing effect was noticed. Distilled water saturated run did not fully plug the pore throats instead it made them narrower and the flow channels became more tortuous. Similarly, 5wt% connate water run had lower pressure drop compared to the 10wt% connate water runs. This means that the pore channels were not significantly reduced thereby allowing more unrestricted flow through the pore matrix.

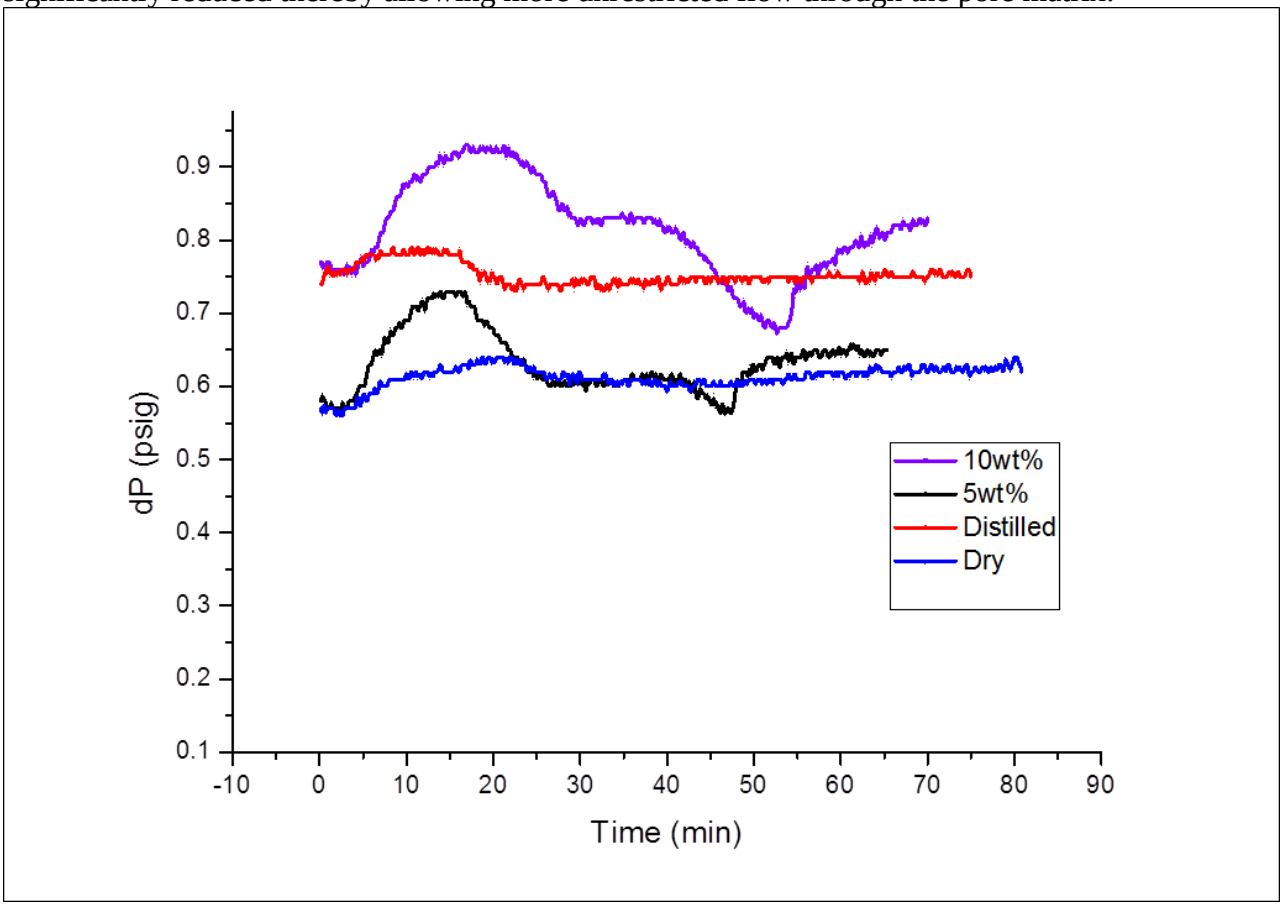

Figure 6 dP changes during all experimental runs at different connate water salinities at 1300 psig and 50°C

3.1.2 Carbon dioxide injection and recovery

Using a simple form of gas material balance and mass conservation, the volume of CO_2 injected, and CO_2 produced can be evaluated to assess the production efficiency of each injection strategy.

$$\sum V_{CO2\ in} = \sum (V_{CO2\ Accumulated} + V_{CO2\ Produced}) \qquad (2)$$

Here, CO_2 was injected at a constant flowrate rate and the effluents produced were recorded and analysed. Produced CO_2 results obtained and analysed are shown in Table 4.

Table 4 CO_2 produced during EGR for all the experimental runs

Tests	Swi %	PV injected	Pv Produced	Pv Accumulated	% CO_2 Stored
10wt%	10	36.10	13.31	22.79	63.13
5wt%	10	36.10	29.44	6.66	18.45
Distilled	10	36.10	27.72	8.38	23.21
Dry	0	36.10	33.65	2.45	6.79

From Table 4, it suffices to say that the experimental run with 10wt% connate water yielded the most significant results in terms of CO_2 storage with 63.05% of the total pore volumes injected stored in the core sample. This is further established and reaffirmed in Figure 7 where the same run yielded the least CO_2 recovered compared to the other runs. Also, the restrictive flow during the run as a result of the sealing effect by the connate water aided the storage of the injected CO_2 which was characterised by the large pressure drop observed during the injection. Next, experimental run with the core sample saturated with distilled water provided stored 23.21% of the total pore volumes injected. This was followed closely by the run with 5wt% connate water and the least efficient storage scenario was the core sample with no connate water with the storage of 6.69% of the total pore volume injected. Given the similar flow behaviour of the injected CO_2 in terms of pressure drops between the distilled water and 5wt% runs, it was expected that the storage efficiency will be very close.

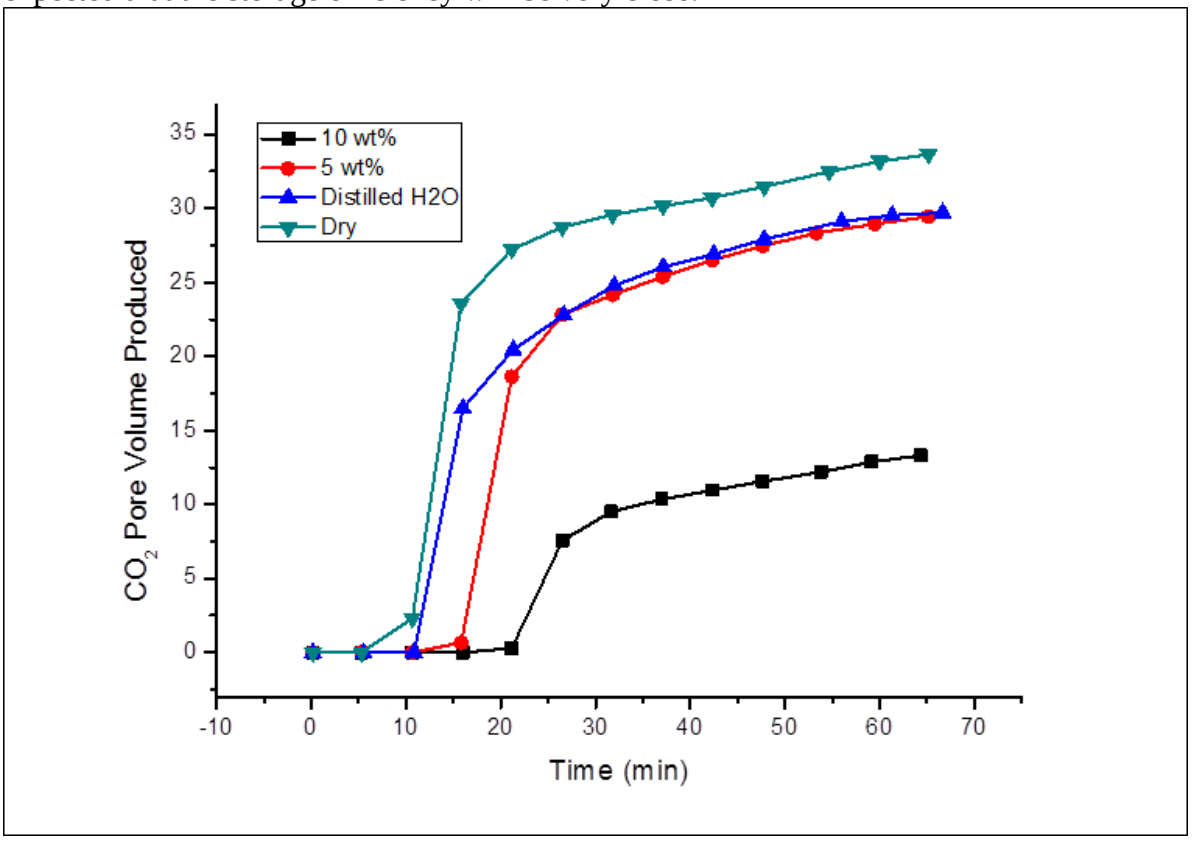

Figure 7 CO_2 volumes recovered in pore volumes as functions of time

Consequently, to assess the displacement efficiency in terms of CH_4 recovery and CO_2 sequestration, Table 2 and Table 3 were combined to produce Figure 8.

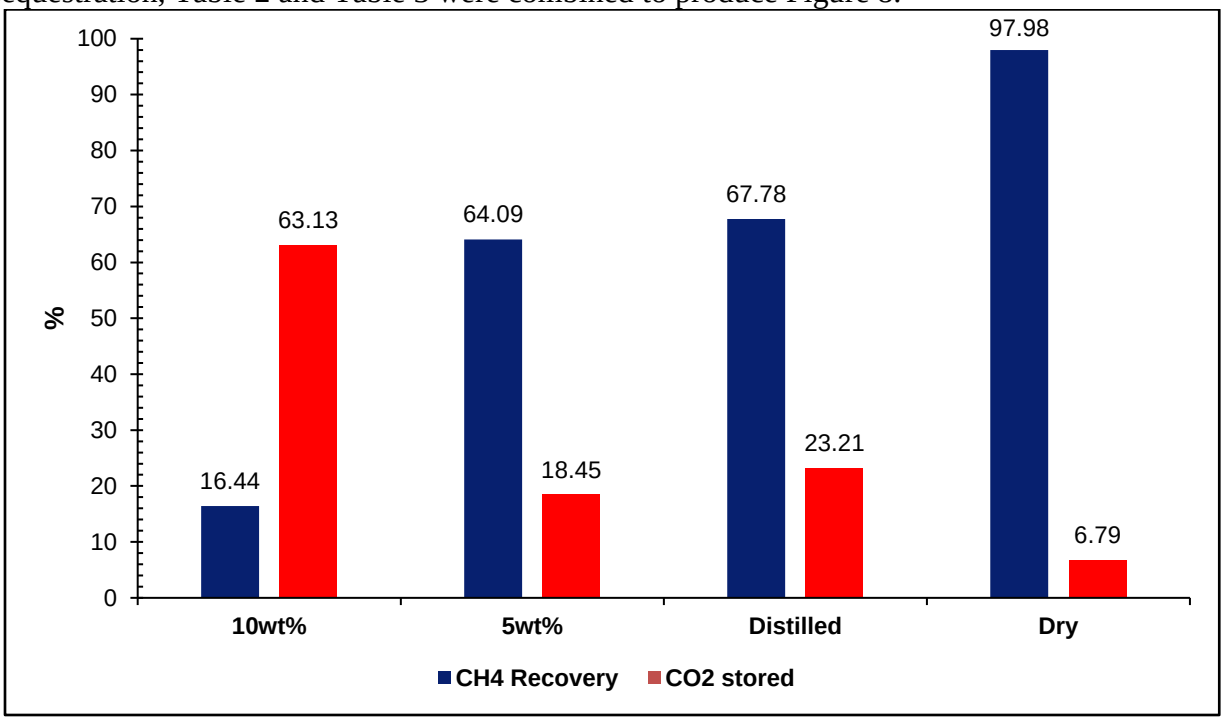

Figure 8 Efficiency of flooding process terms of CO_2 storage and CH_4 recovery

From the Figure, there seem to be an increase in recovery of CH_4 as the salinity decreases, this can be attributed to the pore matrix of the core sample and the flow physics of the fluid as discussed in section 3.1.1. For CO_2 storage, however, the storage efficiency arguably decreased as salinity decreased. That cannot be substantiated because the storage efficiency in the distilled water run is fairly higher than that of the 5wt% run. This could be due to CO_2 solubility in brine and distilled water. Further investigation is thus required to substantiate the claim and expatiate the trend observed.

It is a well-known fact that the CO_2 is highly soluble in water. The mutual solubilities of CO_2 and CH_4 and connate water at different salinities was investigated next using IFT measurement to further drive and explain the narrative already postulated.

3.1.3 IFT Measurements

The experimental fluid-fluid IFT measurement was carried out using the rising bubble technique described in Section 2.2.4.1. This technique capitalises on the buoyancy of the gas bubble with respect to the brine used, in that its ability to rise through the denser fluid is exploited. The IFT measurement is evaluated based on the profile of the gas bubble in the brine created in the IFT cell which is deduced using the Young-Laplace equations:

$$\gamma = \frac{\Delta\rho g d_e^2}{H} \qquad (3)$$

Where

$$\frac{1}{H} = f\left(\frac{d_s}{d_e}\right) \quad (4)$$

$\Delta\rho$ is the density difference between the two fluids, γ is the interfacial tension, g is the acceleration due to gravity, de is equatorial diameter of the drop, ds is the diameter of the bubble at de from the apex, H is the bond number which is a function of the ratio of ds/de. The densities of the phases were evaluated using PVTsim at the test conditions of 1300 psig and 50°C. The IFT was first measured when the external phase (connate water) was not saturated with the drop phase (CO_2) to observe the development and collapse of the bubble generated. The results for all the test fluids are shown in Table 5 where measurements were taken continuously as the bubble shrunk and collapsed.

Table 5 IFT measurement of CO_2 at different brine salinities (1300 psig 50^{O}C)

Time (s)	Distilled Water (mN/m)	5 wt% (mN/m)	10 wt% (mN/m)
0.0	55.23	62.30	65.51
1.0	54.89	61.10	64.53
1.9	52.12	59.89	63.63
2.9	48.11	57.19	63.51
4.0	44.22	55.22	63.48
5.0	38.16	53.45	63.41
6.0	33.67	52.32	63.40
6.9	28.32	51.75	63.38
8.0	24.33	50.11	63.07
9.0	22.12	48.29	62.36

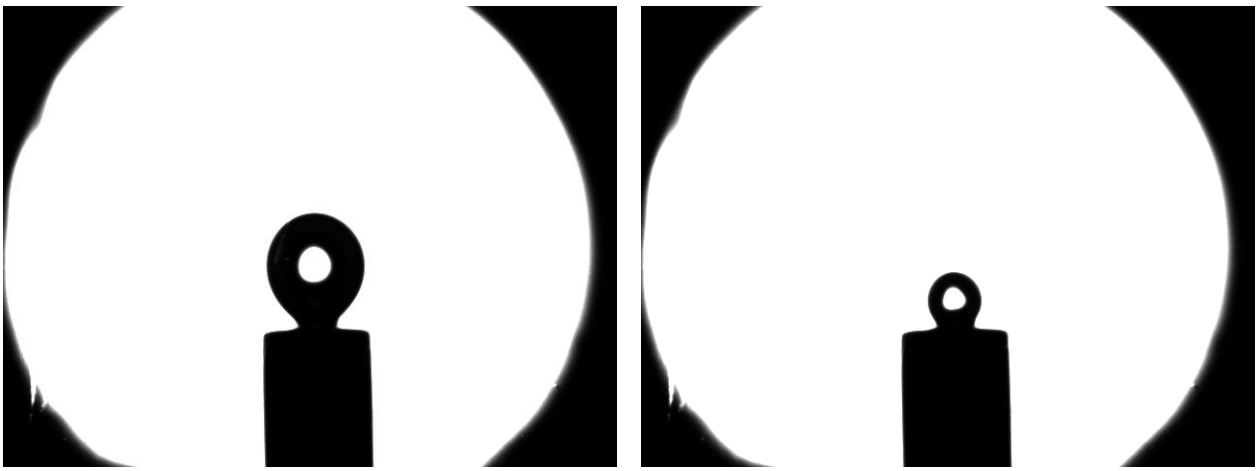

Figure 9 Bubble shrinkage of CO_2 bubble in Distilled water L: Onset R: End (10 seconds interval)

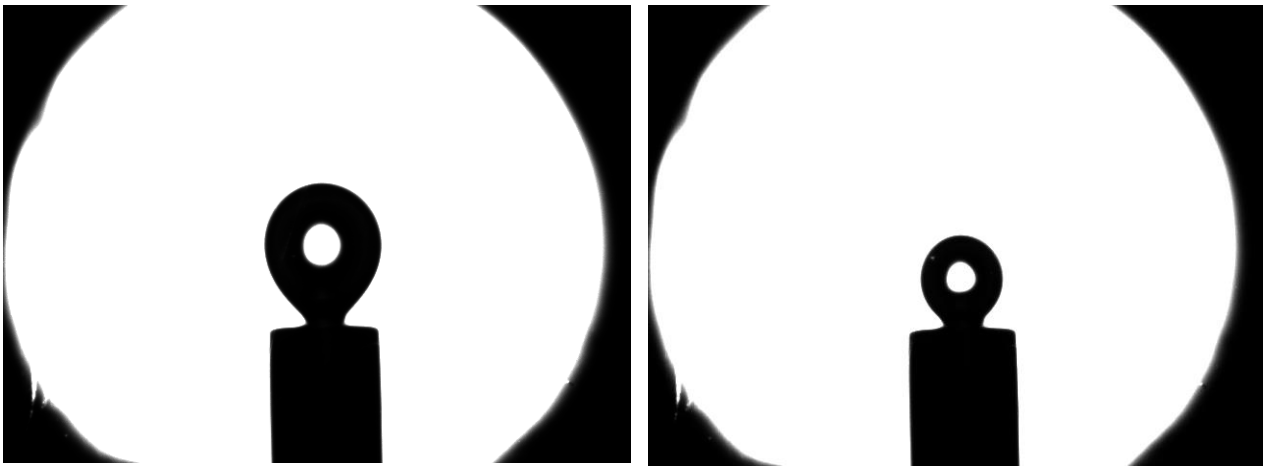

Figure 10 Bubble shrinkage of CO_2 in 5wt% brine L: Onset R: End (10 seconds interval)

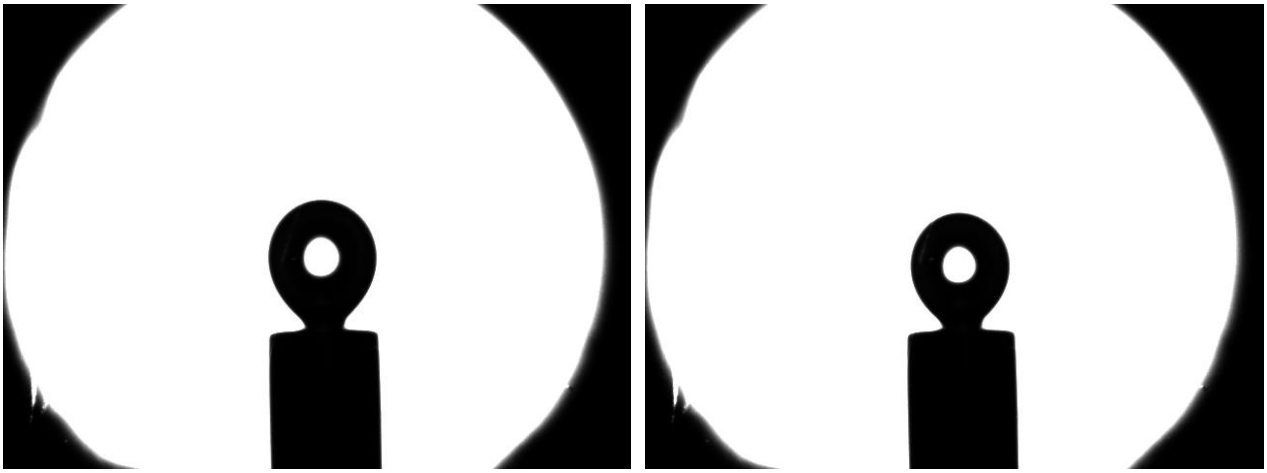

Figure 11 Bubble shrinkage of CO_2 in 10wt% brine L: Onset R: End (10 seconds interval)

The shrinking of the bubble signified the rate of mass transfer over the interface between the gas bubbles generated and brine phase in the cell. As seen in Figure 9, Figure 10, and Figure 11, the rate of shrinkage of the gas bubble is more pronounced in the distilled water experiment and the rate decreased as the salinity of the connate water sample increased. The IFT decreased rapidly in the distilled water which explained the shrinkage observed. However, IFT rate decreased at a slower rate when the salinity increased to 5 w% and even slowest at 10wt% connate water. This is represented graphically in Figure 12.

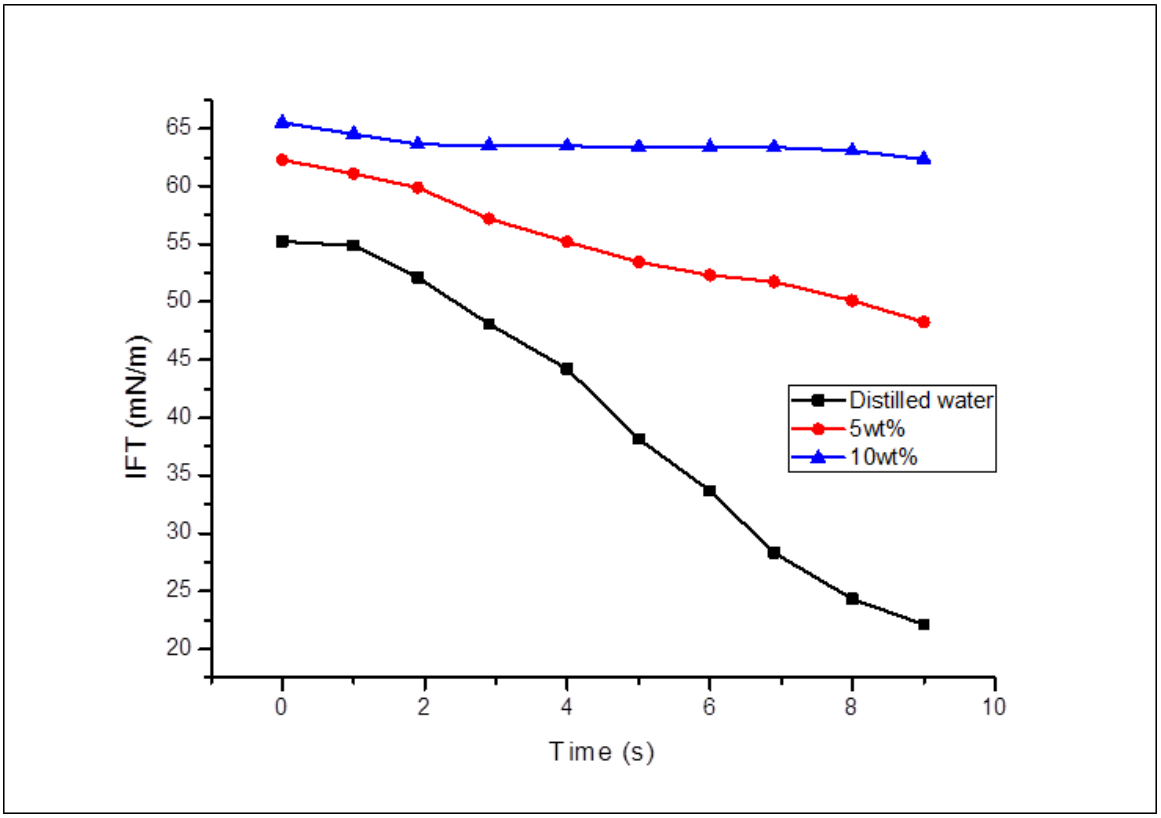

Figure 12 Graphical representation of CO_2 IFT decrease as a function of time at under-saturated aqueous conditions (1300 psig 50^{O}C)

After the results of the rate of shrinkage and IFT variation with time in the unsaturated brine were obtained, the next step was to evaluate CO_2 IFT when the brine was saturated with the injected CH_4. The external phase of the experiment (brine) was saturated with the CH_4 by injecting the gas through the injection needle which pressurised the system to the test pressures. IFT measurements were taken at time intervals at the test conditions. Full equilibrium was achieved after about 3 minutes where the bubble sizes became constant and hence the IFTs. The CH_4 IFT results shown in Figure 13 are similar to those obtained by (Yahaya et al., 2018) at the equilibrium conditions relevant to this work.

From the results, it follows the same trend as that observed when the measuring the CO_2 IFT in brine, in that the rate of IFT decrease is consequential to the brine salinity, with the lowest IFT measured between the CH_4 and the brine. This reaffirms that the higher the salinity of the brine the lower the gas solubility. The graphical representation of the IFT variation with time is shown in Figure 13.

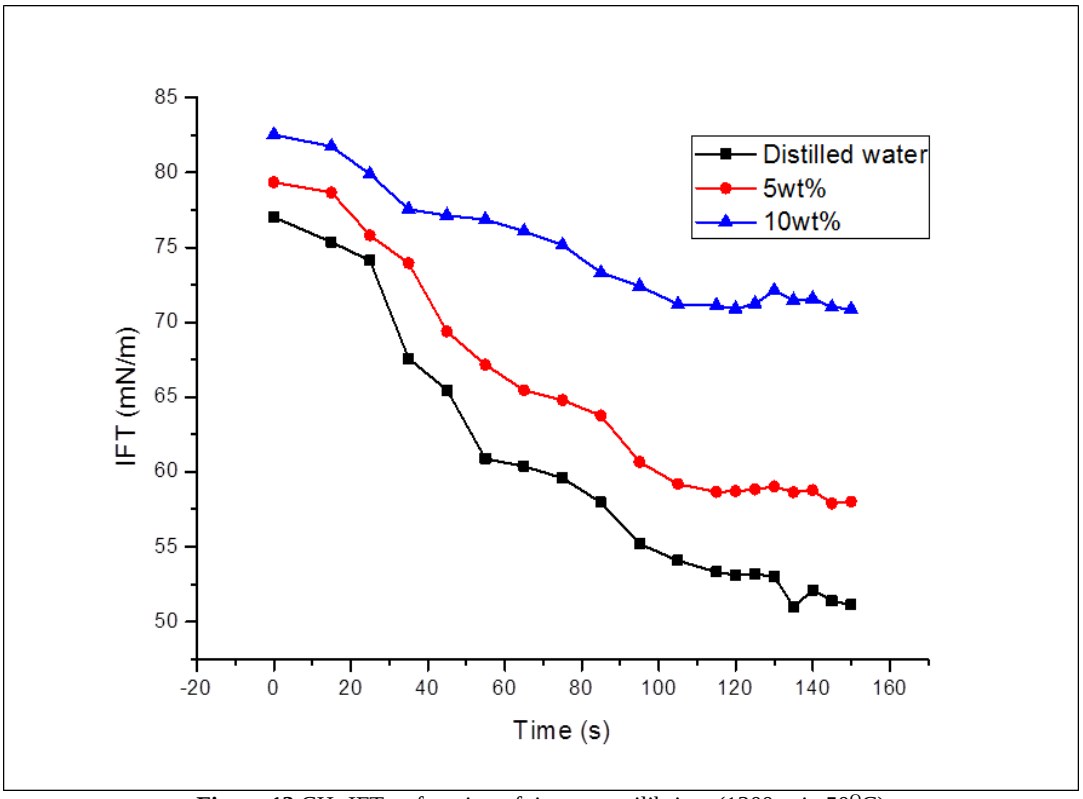

Figure 13 CH_4 IFT as function of time at equilibrium (1300 psig 50^{O}C)

Once the equilibrium between CH_4 and the brine was attained, CO_2 was now injected at the same pressure into the CH_4 saturated brine to evaluate the IFT. This was to simulate the rate of CO_2 dissolution in the reservoir during the displacement. It is noted that the connate water in the reservoir was saturated with the CH_4 prior to injection, so this step in IFT determination of the CO_2 in a CH_4 saturated brine gives a representation of the trends observed in Figure 14.

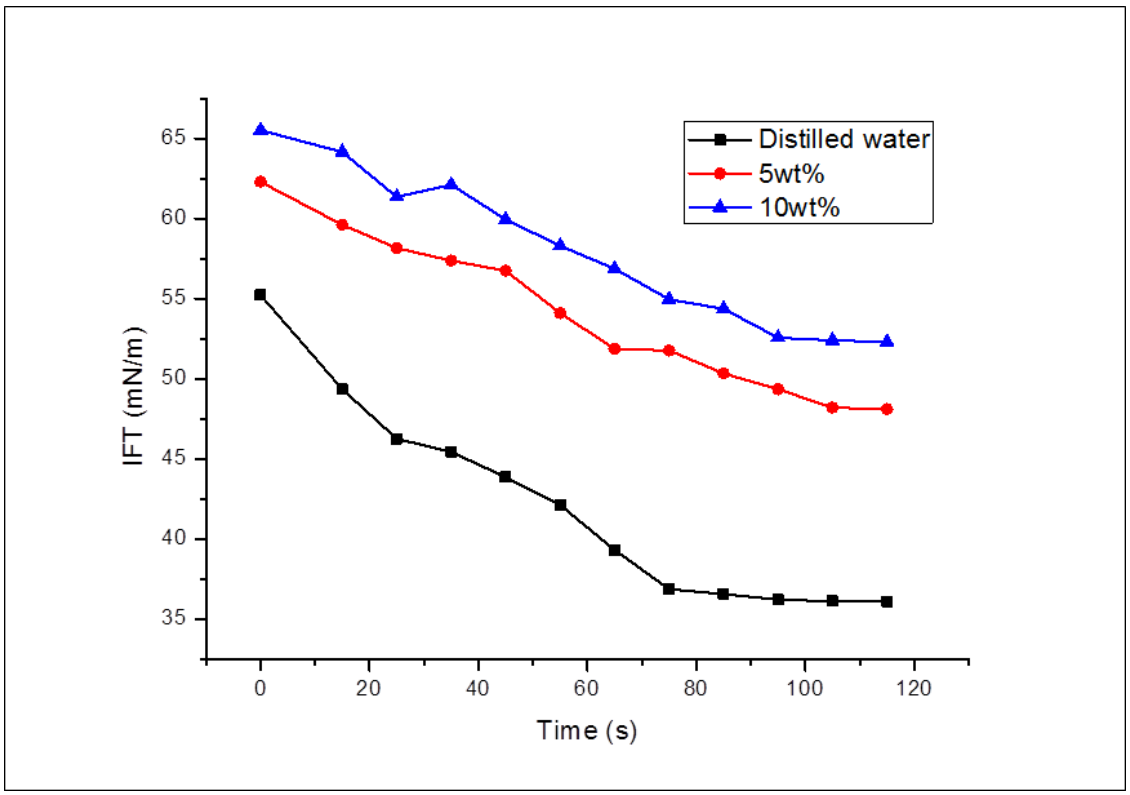

Figure 14 CO_2 IFT as a function of time at saturated conditions

It is clear that the gases had the highest interfacial tension in the brine with the highest salinity and lowest interfacial tension value in distilled water. This explains why more CO_2 seemed to accumulate during the run with distilled water (Table 4 and Figure 8) compared to the run with 5wt%.

The primary trapping mechanisms in the conventional natural gas reservoirs during EGR by CO_2 injection and sequestration are the structural and stratigraphic trapping as seen in Table 4 in the dry run which only about 7% of the injected CO_2 was stored in the core sample. This storage efficiency was considerably increased to about 70% of the injected CO_2 when connate water was introduced into the core sample. This highlights the feasibility that in addition to structural trapping, solubility trapping is realisable during EGR and tends to increase the storage capacity of the conventional natural gas in terms of storage while maintaining substantial recovery of the hydrocarbon resource.

4 CONCLUSION

In this research, Berea sandstone core sample was used as the conventional porous media to carry out a core flooding process to evaluate the production of CH_4 and CO_2 during EGR scenario in the presence of connate water to realise the effects of its presence. CO_2 storage was highest in the run where the connate water salinity was 10wt% which is attributed to the restrictive flow of the injected CO_2 to displace the CH_4 and was characterised by low CO_2 and

high CH_4 recoveries. Here, structural trapping mechanism was dominant and also solubility trapping to an extent. However, solubility trapping mechanism is most pronounced during the distilled (0wt%) and 5wt% salinity runs where both runs had similar CO_2 and CH_4 production, but the distilled water run had the higher CO_2 accumulation. This is due to the higher solubility of the CO_2 in distilled water as seen in their interfacial tensions – with distilled water having a value of *36.12 mN/m* and *48.20 mN/m* for 5wt% brine at the same conditions. CO_2 sequestration during EGR is not just focused on the primary trapping mechanisms of geological sequestration but can also exploit the solubility trapping mechanism in the reservoir connate water to increase the storage capacity. Considering only structural and stratigraphic trapping mechanisms which were simulated using the dry run (no water saturation), only 7% of the injected CO_2 was stored and a substantial volume of 63% of the injected CO_2 was sequestered when solubility trapping was considered by introducing connate water saturation. This goes on to show there is a potential for additional storage capacity through secondary trapping mechanisms. The salinity of the connate water plays a vital role in promoting the trapping – in this case structural trapping which resulted from the density of the connate water sealing off the narrow pore spaces within the pore matrix as evident in the 10wt% connate water run. A substantial volume of CH_4 was recovered in all the cases which is a win-win scenario for the technique. The recovered CH_4 from conventional natural gas reservoir can offset part of the cost of the sequestration process whilst providing good sequestration site CO_2 storage. This study shows that structural and stratigraphic trapping mechanisms are not the only exploitable avenue for CO_2 storage by showcasing the potential of solubility trapping as a secondary trapping mechanism which increases the storage capacity (the limitation) of natural gas reservoir. Future work will entail investigation of effect of other types of salts on this process and at even higher concentrations and saturations.

ACKNOWLEDGEMENTS

The authors wish to acknowledge Petroleum Technology Development Fund (PTDF) for the studentship, and also the Spray Research and Petroleum & Gas research groups of University of Salford, Manchester UK for their consultation.

NOMENCLATURE

CH_4	–	*Methane*
CO_2	–	*Carbon dioxide*
γ	–	*Interfacial Tension IFT (mN/m)*
ρ	–	*Density (g/cm^3)*
g	–	*Acceleration due to gravity (m/s^2)*
de	–	*Bubble equatorial diameter (mm)*
ds	–	*Bubble diameter from bottom tip of bubble to height de (mm)*
H	–	*Bond number*
f	–	*Function*
PV	–	*Pore volume*

REFERENCES

Abba, M.K., Abbas, A.J., Nasr, G.G., 2017. Enhanced Gas Recovery by CO2 Injection and Sequestration: Effect of Connate Water Salinity on Displacement Efficiency, in: SPE Abu Dhabi International Petroleum Exhibition & Conference. https://doi.org/10.2118/188930-

MS
Abba, M.K., Al-Othaibi, A., Abbas, A.J., Nasr, G.G., Mukhtar, A., 2018. Experimental investigation on the impact of connate water salinity on dispersion coefficient in consolidated rocks cores during Enhanced Gas Recovery by CO2 injection. J. Nat. Gas Sci. Eng. 60, 190–201. https://doi.org/10.1016/j.jngse.2018.10.007
Amin, R., Sidiq, H., Kennaird, T., Van der Steen, E., 2010. Gas-gas experimental interfacial tension measurement. Fluid Phase Equilib. 295, 230–236. https://doi.org/10.1016/j.fluid.2010.05.020
Arabloo, M., Ghazanfari, M.H., Rashtchian, D., 2016. Wettability modification, interfacial tension and adsorption characteristics of a new surfactant: Implications for enhanced oil recovery. Fuel 185, 199–210. https://doi.org/10.1016/j.fuel.2016.06.088
Bagalkot, N., Hamouda, A.A., Isdahl, O.M., 2018. Dynamic interfacial tension measurement method using axisymmetric drop shape analysis. MethodsX 5, 676–683. https://doi.org/10.1016/j.mex.2018.06.012
Barati-Harooni, A., Soleymanzadeh, A., Tatar, A., Najafi-Marghmaleki, A., Samadi, S.J., Yari, A., Roushani, B., Mohammadi, A.H., 2016. Experimental and modeling studies on the effects of temperature, pressure and brine salinity on interfacial tension in live oil-brine systems. J. Mol. Liq. 219, 985–993. https://doi.org/10.1016/j.molliq.2016.04.013
Burton, M., Kumar, N., Bryant, S.L., 2009. CO2 injectivity into brine aquifers: Why relative permeability matters as much as absolute permeability. Energy Procedia 1, 3091–3098. https://doi.org/10.1016/j.egypro.2009.02.089
Cantrell, K.J., Brown, C.F., 2014. Source term modeling for evaluating the potential impacts to groundwater of fluids escaping from a depleted oil reservoir used for carbon sequestration. Int. J. Greenh. Gas Control 27, 139–145. https://doi.org/10.1016/j.ijggc.2014.05.009
Chen, L., Wang, M., Kang, Q., Tao, W., 2018. Pore scale study of multiphase multicomponent reactive transport during CO2dissolution trapping. Adv. Water Resour. 116, 208–218. https://doi.org/10.1016/j.advwatres.2018.02.018
Chow, Y.T.F., Maitland, G.C., Trusler, J.P.M., 2016. Interfacial tensions of the (CO2 + N2 + H2O) system at temperatures of (298 to 448) K and pressures up to 40 MPa. J. Chem. Thermodyn. 93, 392–403. https://doi.org/10.1016/j.jct.2015.08.006
Dehghan, A.A., Masihi, M., Ayatollahi, S., 2015. Phase behavior and interfacial tension evaluation of a newly designed surfactant on heavy oil displacement efficiency; effects of salinity, wettability, and capillary pressure. Fluid Phase Equilib. 396, 20–27. https://doi.org/10.1016/j.fluid.2015.03.028
Ding, S., Xi, Y., Jiang, H., Liu, G., 2018. CO2storage capacity estimation in oil reservoirs by solubility and mineral trapping. Appl. Geochemistry 89, 121–128. https://doi.org/10.1016/j.apgeochem.2017.12.002
Duan, S., Gu, M., Du, X., Xian, X., 2016. Adsorption Equilibrium of CO2 and CH4 and Their Mixture on Sichuan Basin Shale. Energy and Fuels 30, 2248–2256. https://doi.org/10.1021/acs.energyfuels.5b02088
Duchateau, C., Broseta, D., 2012. A simple method for determining brine-gas interfacial tensions. Adv. Water Resour. 42, 30–36. https://doi.org/10.1016/j.advwatres.2012.03.008
Ganjdanesh, R., Hosseini, S.A., 2017. Geologic Carbon Storage Capacity Estimation Using Enhanced Analytical Simulation Tool (EASiTool). Energy Procedia 114, 4690–4696. https://doi.org/10.1016/j.egypro.2017.03.1601
Jia, W., Pan, F., Dai, Z., Xiao, T., McPherson, B., 2017. Probabilistic Risk Assessment of

CO2Trapping Mechanisms in a Sandstone CO2-EOR Field in Northern Texas, USA. Energy Procedia 114, 4321–4329. https://doi.org/10.1016/j.egypro.2017.03.1581
Kalra, S., Wu, X., 2014. CO2 injection for Enhanced Gas Recovery. SPE West. North Am. Rocky Mt. … 16–18.
Kamari, A., Pournik, M., Rostami, A., Amirlatifi, A., Mohammadi, A.H., 2017. Characterizing the CO2-brine interfacial tension (IFT) using robust modeling approaches: A comparative study. J. Mol. Liq. 246, 32–38. https://doi.org/10.1016/j.molliq.2017.09.010
Kashefi, K., Pereira, L.M.C., Chapoy, A., Burgass, R., Tohidi, B., 2016. Measurement and modelling of interfacial tension in methane/water and methane/brine systems at reservoir conditions. Fluid Phase Equilib. 409, 301–311. https://doi.org/10.1016/j.fluid.2015.09.050
Khaksar Manshad, A., Olad, M., Taghipour, S.A., Nowrouzi, I., Mohammadi, A.H., 2016. Effects of water soluble ions on interfacial tension (IFT) between oil and brine in smart and carbonated smart water injection process in oil reservoirs. J. Mol. Liq. 223, 987–993. https://doi.org/10.1016/j.molliq.2016.08.089
Li, B., Tchelepi, H.A., Benson, S.M., 2013. Influence of capillary-pressure models on CO2 solubility trapping. Adv. Water Resour. 62, 488–498. https://doi.org/10.1016/j.advwatres.2013.08.005
Mijic, A., LaForce, T.C., Muggeridge, A., 2014. Co2 injectivity in saline aquifers: the impact of non darcy flow, phase misciibility and gas compressibility. Water Resour. Res. WR014893, 4163–4185. https://doi.org/10.1002/2013WR014893.Received
Mohammad Salehi, M., Omidvar, P., Naeimi, F., 2017. Salinity of injection water and its impact on oil recovery absolute permeability, residual oil saturation, interfacial tension and capillary pressure. Egypt. J. Pet. 26, 301–312. https://doi.org/10.1016/j.ejpe.2016.05.003
Mutailipu, M., Liu, Y., Jiang, L., Zhang, Y., 2018a. Measurement and estimation of CO2–brine interfacial tension and rock wettability under CO2 sub- and super-critical conditions. J. Colloid Interface Sci. https://doi.org/10.1016/j.jcis.2018.09.031
Mutailipu, M., Liu, Y., Jiang, L., Zhang, Y., 2018b. Measurement and estimation of CO2–brine interfacial tension and rock wettability under CO2 sub- and super-critical conditions. J. Colloid Interface Sci. 534, 605–617. https://doi.org/10.1016/j.jcis.2018.09.031
Nakajima, T., Xue, Z., 2017. Trapping Mechanisms in Field Scale: Results from Nagaoka Geologic CO2Storage Site. Energy Procedia 114, 5015–5022. https://doi.org/10.1016/j.egypro.2017.03.1650
Oh, J., Kim, K.Y., Han, W.S., Park, E., 2017. Transport of CO2in heterogeneous porous media: Spatio-temporal variation of trapping mechanisms. Int. J. Greenh. Gas Control 57, 52–62. https://doi.org/10.1016/j.ijggc.2016.12.006
Pereira, L.M.C., Chapoy, A., Burgass, R., Tohidi, B., 2017. Interfacial tension of CO2+ brine systems: Experiments and predictive modelling. Adv. Water Resour. 103, 64–75. https://doi.org/10.1016/j.advwatres.2017.02.015
Rashid, S., Harimi, B., Hamidpour, E., 2017. Prediction of CO2-Brine interfacial tension using a rigorous approach. J. Nat. Gas Sci. Eng. 45, 108–117. https://doi.org/10.1016/j.jngse.2017.05.002
Raza, A., Rezaee, R., Bing, C.H., Gholami, R., Hamid, M.A., Nagarajan, R., 2016. Carbon dioxide storage in subsurface geologic medium: A review on capillary trapping mechanism. Egypt. J. Pet. 25, 367–373. https://doi.org/10.1016/j.ejpe.2015.08.002
Sminchak, J.R., Babarinde, O., Gupta, N., 2017. Integrated Analysis of Geomechanical Factors for Geologic CO2Storage in the Midwestern United States. Energy Procedia 114, 3267–

3272. https://doi.org/10.1016/j.egypro.2017.03.1458
Stukan, M., Abdallah, W., East, S.M., 2012. Interfacial Tension (IFT) and Surface Alteration Interplay. Spe 11–14. https://doi.org/10.2118/161279-ms
Valle, L.M., Rodríguez, R., Grima, C., Martínez, C., 2018. Effects of supercritical CO2 injection on sandstone wettability and capillary trapping. Int. J. Greenh. Gas Control 78, 341–348. https://doi.org/10.1016/j.ijggc.2018.09.005
Valle, L M, Rodríguez, R., Grima, C., Martínez, C., 2018. Effects of supercritical CO2 injection on sandstone wettability and capillary trapping. Int. J. Greenh. Gas Control 78, 341–348. https://doi.org/10.1016/j.ijggc.2018.09.005
van der Meer, B., 2005. Carbon dioxide storage in natural gas reservoirs. Oil Gas Sci. Technol. 60, 527–536. https://doi.org/10.2516/ogst:2005035
Xiao, T., McPherson, B., Pan, F., Esser, R., Jia, W., Bordelon, A., Bacon, D., 2016. Potential chemical impacts of CO 2 leakage on underground source of drinking water assessed by quantitative risk analysis. Int. J. Greenh. Gas Control 50, 305–316. https://doi.org/10.1016/j.ijggc.2016.04.009
Yahaya, A.A., Akpan, E.U., Enyi, G.C., Nasr, G.G., Abbas, J., 2018. Experimental investigation of methane-water and methane-brine IFT measurements using pendant drop (rising bubble) method Journal of Engineering Technology. J. Eng. Technol. 6, 394–407.
Yasuda, K., Mori, Y.H., Ohmura, R., 2015. Interfacial tension measurements in water-methane system at temperatures from 278.15 K to 298.15 K and pressures up to 10 MPa. Fluid Phase Equilib. 413, 170–175. https://doi.org/10.1016/j.fluid.2015.10.006

APPENDIX

Error analysis of the core flooding runs											
Dry Runs			**Distilled water**			**5wt% NaCl**			**10wt% NaCl**		
Time (min)	**Average Mol. Frac CO_2 (%)**	**Standard Deviation CO_2 (%)**	**Time (min)**	**Average Mol. Frac CO_2 (%)**	**Standard Deviation (%)**	**Time (min)**	**Average Mol. Frac CO_2 (%)**	**Standard Deviation (%)**	**Time (min)**	**Average Mol. Frac CO_2 (%)**	**Standard Deviation (%)**
0.17	0.0	0.0	0.17	0.0	0.0	0.16	0.0	0.0	0.15	0.0	0.0
5.32	0.0	0.0	5.33	0.0	0.0	5.33	0.0	0.0	5.49	0.0	0.0
10.66	0.0	0.0	10.67	2.3	2.5	10.67	1.7	2.9	10.83	6.3	4.7
15.99	1.0	1.0	15.82	6.5	3.7	15.83	61.8	2.8	15.99	70.7	4.0
21.16	4.9	4.5	21.16	70.8	11.0	21.16	74.6	3.1	21.32	78.6	3.2
26.49	70.2	4.0	26.49	89.2	3.3	26.49	84.2	4.1	26.66	82.8	2.6
31.66	81.1	3.8	31.83	92.0	1.7	31.82	90.4	2.5	31.98	85.1	1.0
37.01	91.0	1.0	37.16	94.7	1.4	37.16	94.1	2.4	37.16	86.6	1.5
42.32	93.5	1.3	42.33	96.6	0.7	42.32	95.8	2.1	42.48	88.0	1.0
47.66	96.1	0.8	47.67	97.6	0.6	47.82	97.0	1.0	47.82	89.5	0.4
53.82	97.5	0.5	53.33	97.9	0.8	54.66	97.0	1.0	55.98	90.3	0.9
59.16	98.5	0.4	59.49	98.2	0.3	60.01	97.3	1.2	61.33	90.6	1.2
64.32	98.5	0.5	65.16	98.2	0.3	65.16	97.5	1.2	66.66	90.8	1.4

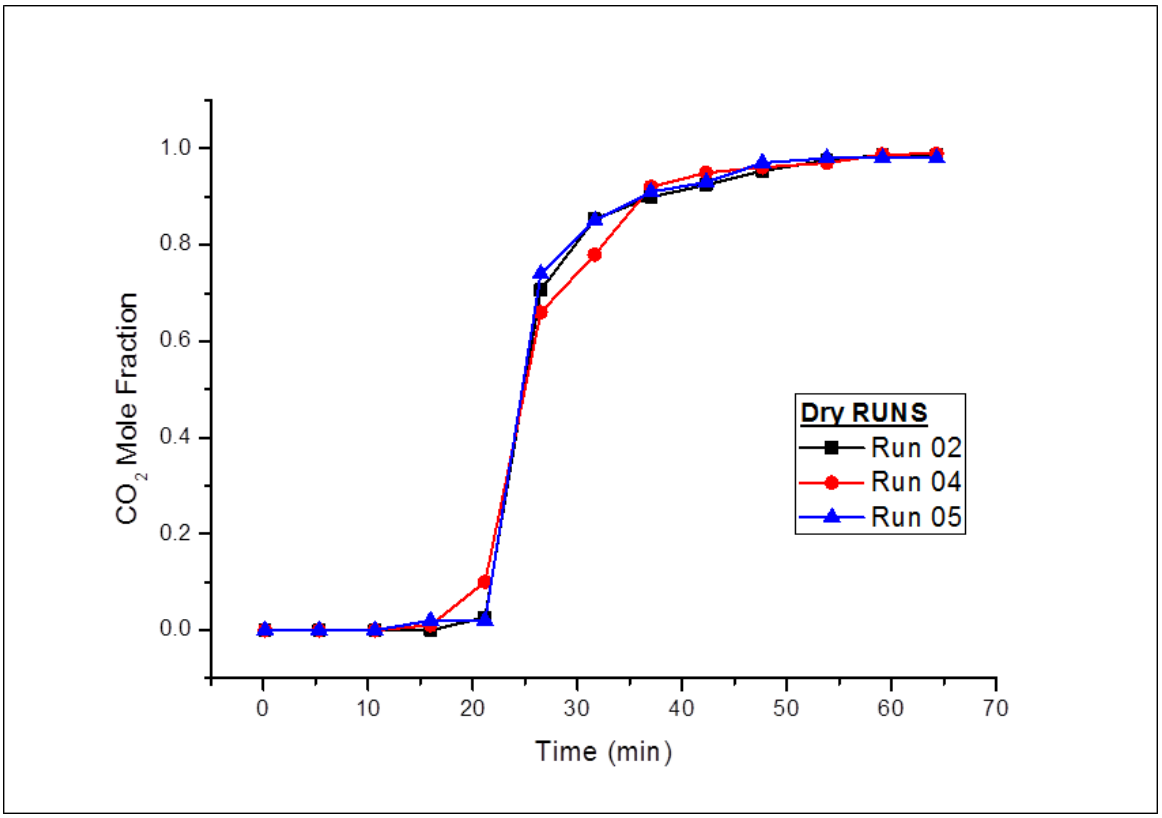
1.0
0.8
0.6
0.4
0.2
0.0
CO_2 Mole Fraction
0
10
20
30
40
50
60
70
Time (min)
Dry RUNS
Run 02
Run 04
Run 05

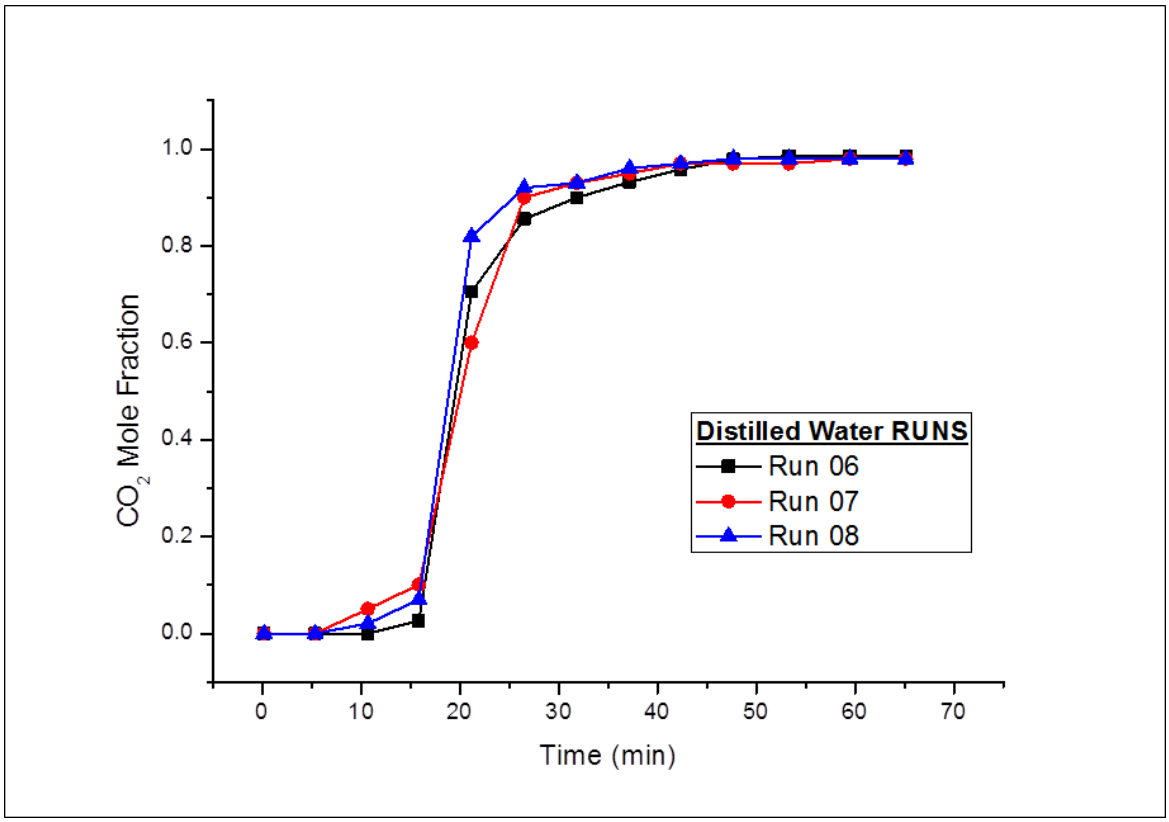
1.0
0.8
0.6
0.4
0.2
0.0
CO_2 Mole Fraction
0
10
20
30
40
50
60
70
Time (min)
Distilled Water RUNS
Run 06
Run 07
Run 08

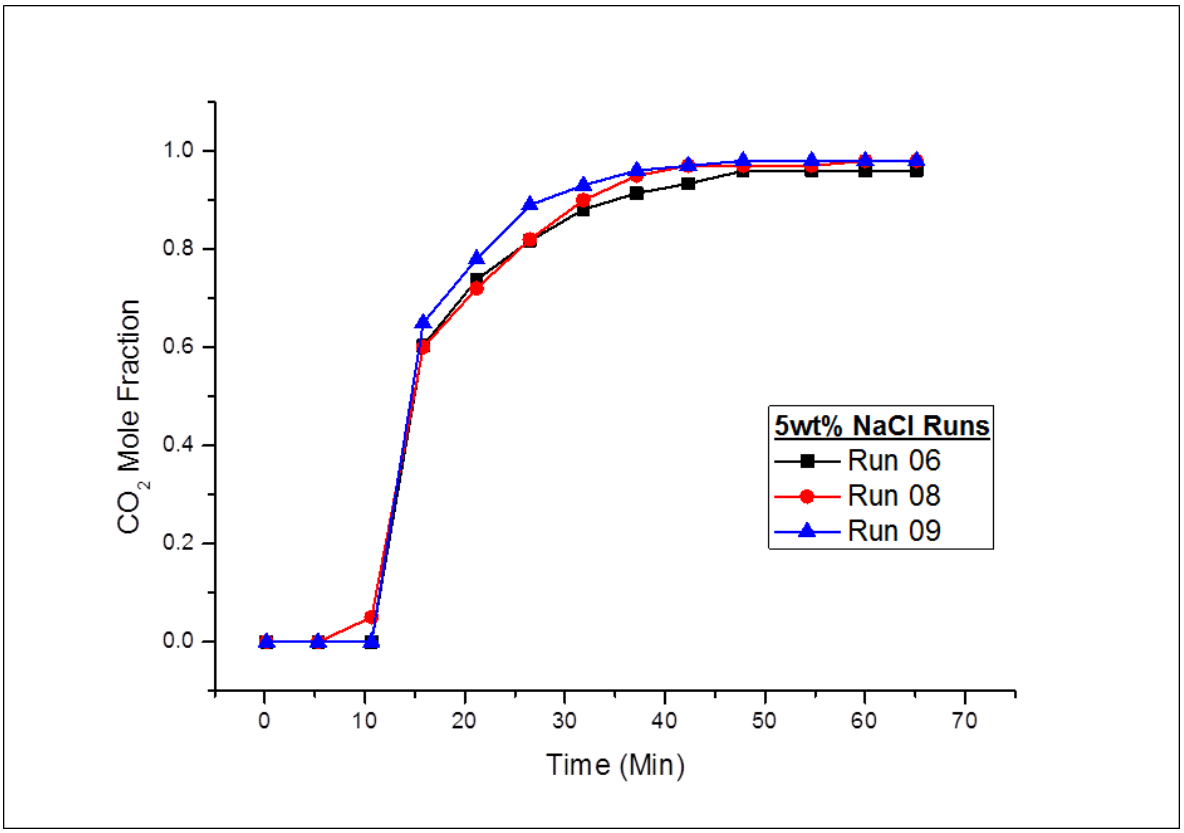
1.0
0.8
0.6
0.4
0.2
0.0
CO_2 Mole Fraction
0
10
20
30
40
50
60
70
Time (Min)
5wt% NaCl Runs
Run 06
Run 08
Run 09

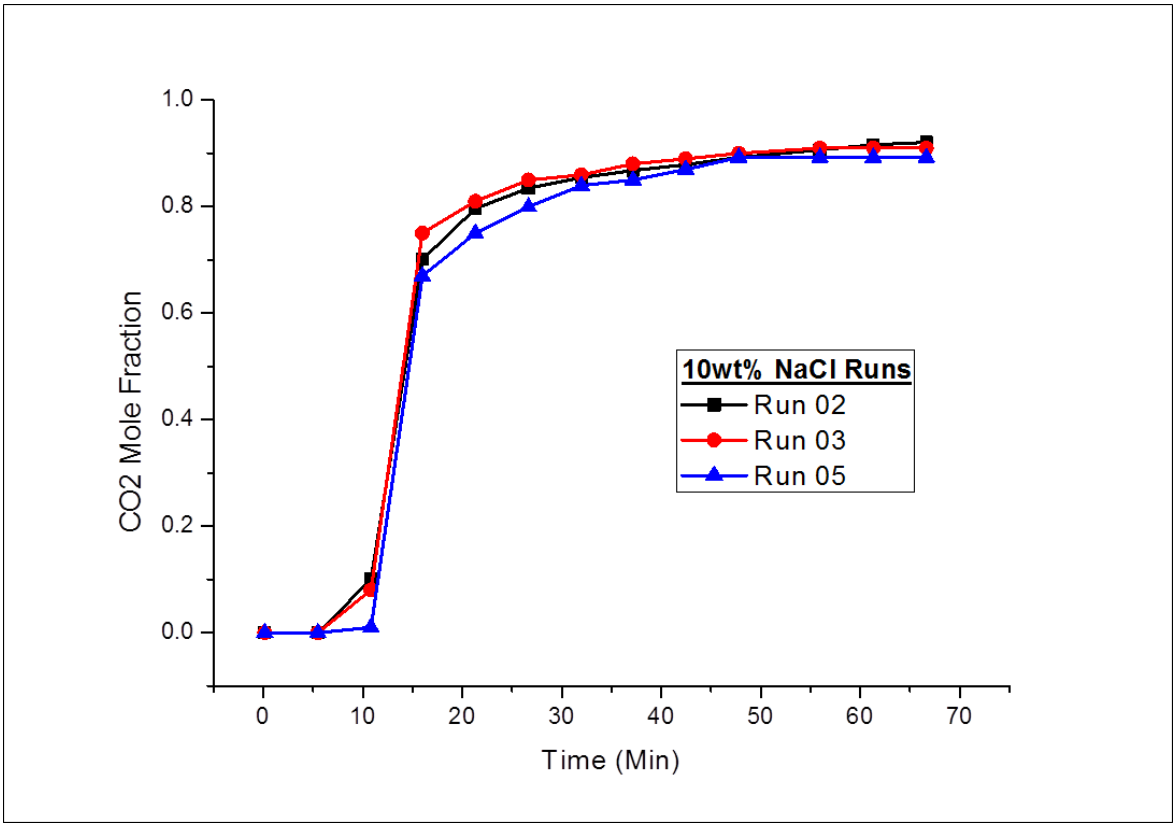
1.0
0.8
0.6
0.4
0.2
0.0
CO2 Mole Fraction
0
10
20
30
40
50
60
70
Time (Min)
10wt% NaCl Runs
Run 02
Run 03
Run 05